Hot Deformation Behaviors and Processing Maps of 2024 Aluminum Alloy in As-cast and Homogenized States

Liang Chen, Guoqun Zhao, Jie Gong, Xiaoxue Chen, and Mengmeng Chen

The isothermal hot compression tests of as-cast and homogenized 2024 aluminum alloy were carried out under wide range of deformation temperatures (623-773 K) and strain rates (0.001-10 s^{-1}). The constitutive equations for both initial states were established based on Arrhenius model, and the processing maps were constructed based on the dynamic material model. The results show that the flow stress of samples is evidently affected by both the strain rate and deformation temperature, and the flow stress in homogenized state is always higher than that in as-cast state. Through calculating the correlation coefficient (R) and average absolute relative error of the established constitutive equations, it indicates that Arrhenius model can only provide a rough estimation on the flow stress. However, a much more precise value of the flow stress was obtained by introducing the strain compensation into Arrhenius model, since the effects of strain on the material constants were well considered. Furthermore, according to the processing maps, a suggested range of deformation temperature and strain rate for hot forming process were given then: temperature range 710-773 K and strain rate range 0.001-1 s^{-1} for as-cast state, and temperature range 680-773 K and strain rate range 0.003-0.22 s^{-1} for homogenized state.

1. Introduction

In recent decades, aluminum alloys, as one of lightweight materials have attracted extensive attentions, due to their characteristics of light-weight, high strength to weight ratio, high corrosion resistance, and easy recycling. Till now, various kinds of aluminum alloys with different compositions have been developed. Among them, 2024 aluminum alloy with high strength, good corrosion resistance, and excellent high temperature characteristics has been widely used in fields of aerospace and aviation (Ref 1). Moreover, 2024 aluminum alloy is usually subjected to hot forming processes, such as forging, hot rolling, and extrusion because of its low plasticity at room temperature.

In practice, the hot forming process should be optimized to obtain the desired products with high dimensional accuracy, specified microstructure, and excellent mechanical properties. However, the complexity of hot deformation behaviors of aluminum alloys makes it extremely difficult to get the optimum forming conditions. One reason is that work hardening and dynamic softening take place simultaneously during the hot forming process. The other reason is that the flow stress is affected by the applied deformation conditions significantly. A deeper understanding of hot deformation behaviors of aluminum alloys is essential for optimizing the hot forming process and controlling the final microstructure. Thus, many research works

Liang Chen, Guoqun Zhao, Jie Gong, Xiaoxue Chen, and **Mengmeng Chen**, Key Laboratory for Liquid-Solid Structural Evolution and Processing of Materials (Ministry of Education), Shandong University, Jinan 250061, China. Contact e-mails: chenliang@sdu.edu.cn and zhaogq@sdu.edu.cn.

have been carried out on the constitutive modeling and processing maps of aluminum alloys in the past decade.

The constitutive equations were developed to describe the relationships between the flow stress and the strain, strain rate, and deformation temperature. These equations can be applied to estimate the required load or power for hot forming processes and to predict the material flow pattern (Ref 2). On the other hand, with the development of computer technology, many studies on metal forming processes have been done with the help of the numerical simulation (Ref 3-5). However, only when a proper constitutive equation is embedded, the simulated results can be truly reliable. Thus, a number of researchers have made efforts on establishing constitutive equations of aluminum alloys based on the experimental measured true stress-strain data (Ref 6-13). Among many constitutive models, the Arrhenius model has been proved to own high prediction accuracy of the flow stress, since it considered coupled effects of strain rate and deformation temperature. Moreover, strain compensated Arrhenius model has also been developed by introducing the influence of strain (Ref 10-13).

Processing map is another important approach to describe the workability of metals and alloys. Prasad et al. (Ref 14) firstly proposed processing maps based on the theory of dynamic material model (DMM). Processing maps consist of stable and instable domains, by which the plastic deformation mechanisms in various conditions could be predicted, and the instable deformation zones related to the phenomenon of the flow instability could be avoided (Ref 15). Therefore, processing maps are considerably important in optimizing hot working process and controlling microstructure (Ref 16). In recent years, a number of processing maps for various aluminum alloys have been established (Ref 17-22).

Due to the wide application of wrought 2024 aluminum alloy, some researchers have attempted to study its hot deformation behavior. Malas et al. (Ref 23) presented the activation energy map and stability map of 2024 aluminum alloy with different initial microstructures, e.g., as-cast and wrought states. Ebrahimi

et al. (Ref 24) analyzed the flow stress differences in supersaturated and annealed 2024 aluminum alloys. Bhimavarapu et al. (Ref 20) developed 2D and 4D processing maps of as-cast 2024 aluminum alloys based on hot compression tests. However, it should be noticed that the constitutive equations were not clearly given in these early reports, especially for as-cast and homogenized 2024 aluminum alloys.

In this study, the constitutive equations and processing maps of as-cast and homogenized 2024 aluminum alloys were respectively developed. The initial microstructures were carefully examined and compared. The isothermal hot compression tests were carried out, and the true stress-strain data at various deformation temperatures and strain rates were measured. The constitutive equations based on Arrhenius model with and without strain compensation were derived for both initial states, and the prediction accuracy of these equations was quantitatively evaluated by analyzing the correlation coefficient (R) and average absolute relative error (AARE). The processing maps were established based on DMM, and the optimum hot working conditions for both initial states were given. The results can help engineers determine the appropriate forming conditions and perform numerical simulation on hot forming processes of 2024 aluminum alloy, which should have important engineering meanings.

2. Experimental Procedure

2024 aluminum alloy with chemical composition (wt.%) of Al-4.4Cu-1.32 Mg-0.5Mn-0.42Si-0.28Zn is used in the present study. The as-cast and homogenized 2024 aluminum alloys were received from a local aluminum extrusion company, in the form of round rod with a diameter of 325 mm. The homogenization was performed at 763 K for 18 h, and then cooled to room temperature in the air.

The hot compression tests were performed using Gleeble-1500 thermo-simulation machine. The cylindrical specimens with a height of 15 mm and diameter of 10 mm were machined from the aluminum alloy rod. As the size of as-received round rod is large, the initial microstructure in different positions varied significantly, especially for the as-cast one. In order to ensure the microstructure consistency of each specimen tested in this study, the specimens were cut along a concentric circle from the as-received rod, as depicted in Fig. 1. Totally, 20 hot compression tests were carried out at various temperatures from 623 to 773 K at an interval of 50 K and the strain rate varied
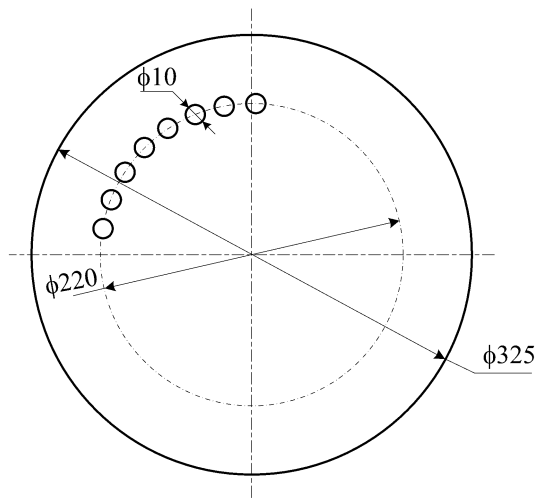

Fig. 1 Schematic drawing of the cutting positions of hot compression tests specimens. (Unit: mm)
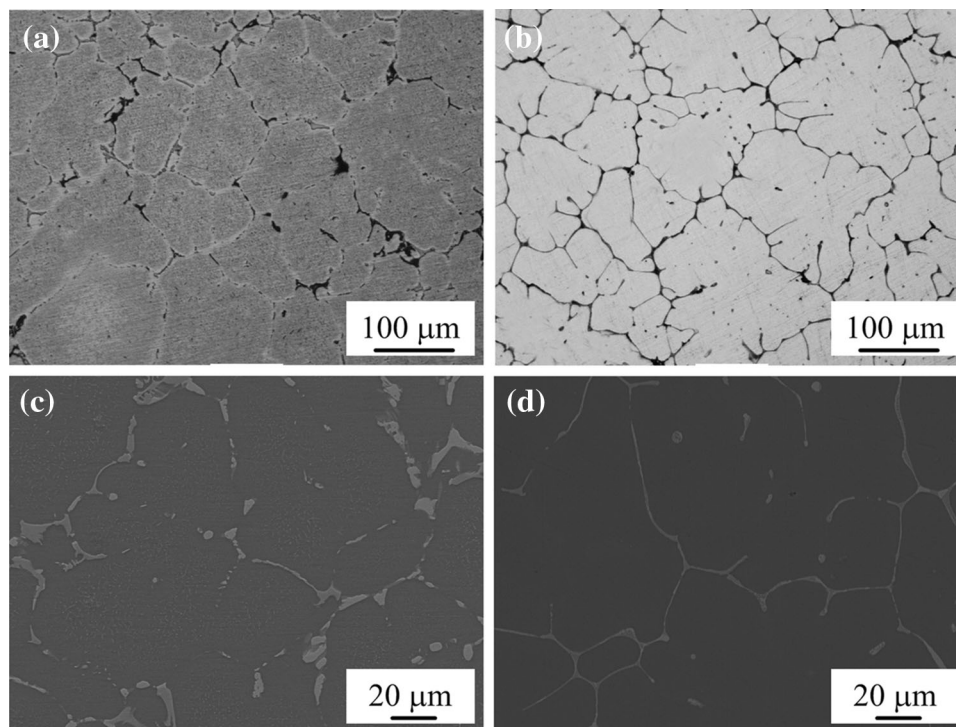

Fig. 2 Initial microstructure of the (a), (c) as-cast and (b), (d) homogenized 2024 aluminum alloy
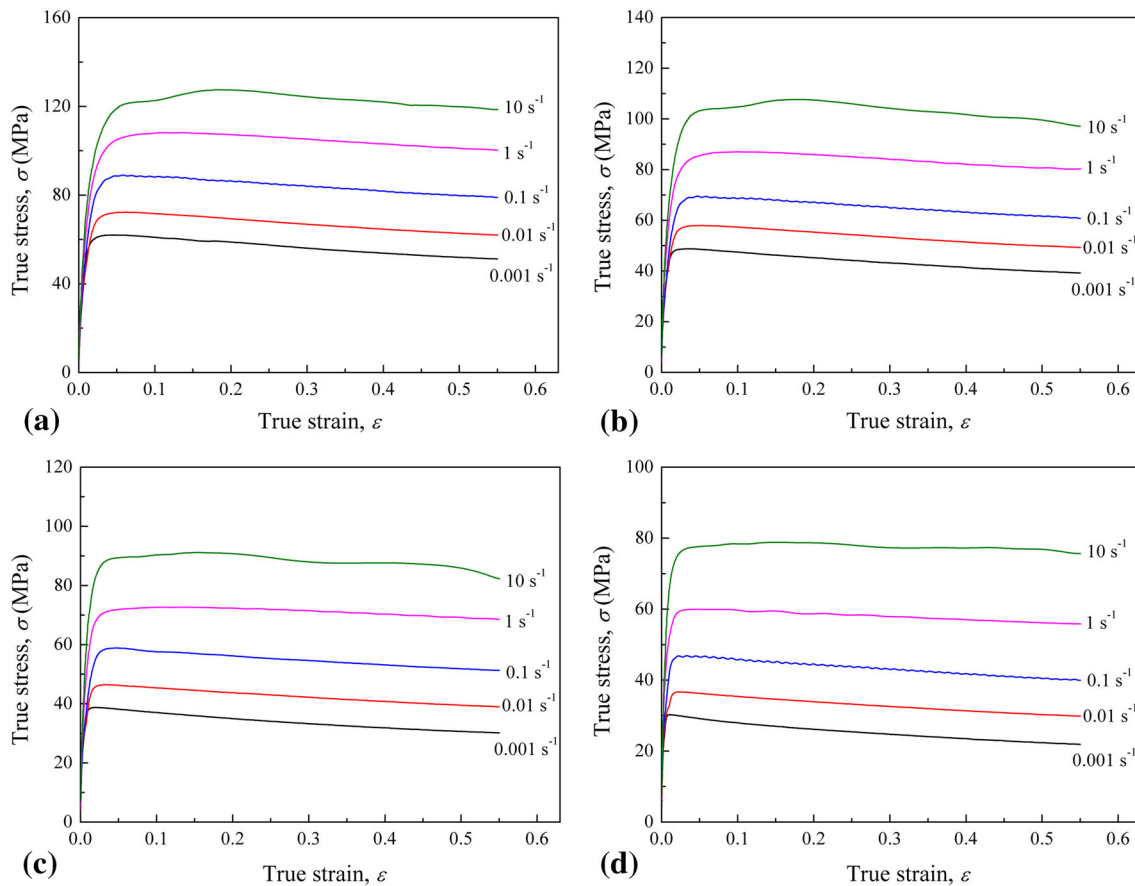
Fig. 3 True stress-strain curves of as-cast 2024 aluminum alloy with various strain rates and at the deformation temperatures of (a) 623 K, (b) 673 K, (c) 723 K, and (d) 773 K

from 0.001 to 10 s^{-1}. The specimens were firstly heated to the deformation temperature with a heating rate of 10 K/s, and then were kept isothermally for 180 s to eliminate the temperature gradient of specimens. The K type thermocouple was spot welded in the middle of the specimen to accurately measure the temperature of specimen. The graphite foils were used as lubricant between the specimen and the anvil to minimize the negative effects of interfacial friction on the true stress-strain data. The barreling of specimen is slight in this study, and thus the effects of friction on flow stress were neglected. All specimens after deformation were water quenched immediately. The force-stroke data during compression tests were automatically recorded and transformed into true stress-strain curves.

The initial and several deformed specimens were cut along the compression axis, following by the grinding, polishing, and then etching. The etching solution was mixed with 1.0 mL HF, 1.5 mL HCl, 2.5 mL HNO$_3$, and 95 mL H$_2$O. The microstructure of samples was examined by optical microscope (OM) and scanning electron microscope (SEM).

3. Results and Discussion

3.1 Initial Microstructure

Figure 2 shows the microstructure of as-cast and homogenized 2024 aluminum alloy before hot compression tests. Coarse equiaxed grains can be obviously observed in both

initial states, as shown in Fig. 2(a) and (b), which indicates the homogenization treatment has little influence on the grain size and morphology. It can be seen in Fig. 2(c) that the as-cast sample has a multi-phase microstructure consisting of α-Al matrix and grain boundary (GB) phases. According to the previous report (Ref 24), the GB phases might be θ-Al$_2$Cu and S-Al$_2$CuMg precipitates, which were formed due to the alloying segregation during casting process. After homogenization, the GB phases became narrow and formed a net structure, as shown in Fig. 2(d). The thinning mechanism of GB phases during homogenization has been demonstrated by Eivani et al. (Ref 25) that the solubility of precipitates in α-Al matrix increases at higher temperature resulting in dissolving partial GB phases. Regarding to the formation of net structure, one possible reason is due to the slow cooling rate inside the aluminum rod. It has been mentioned that the investigated aluminum rod has large size, besides the air cooling was employed after homogenization, both of which lead to the slow cooling rate inside aluminum rod. During slow cooling process, partial solutes precipitated again along the GB or previous dendrite boundary, and the net structure of GB phases was formed.

3.2 Flow Stress Behavior

The true stress-strain curves of as-cast and homogenized 2024 aluminum alloy obtained from hot compression tests are presented in Fig. 3 and 4, respectively. It can be seen that the flow stress increases dramatically with increasing strain at early
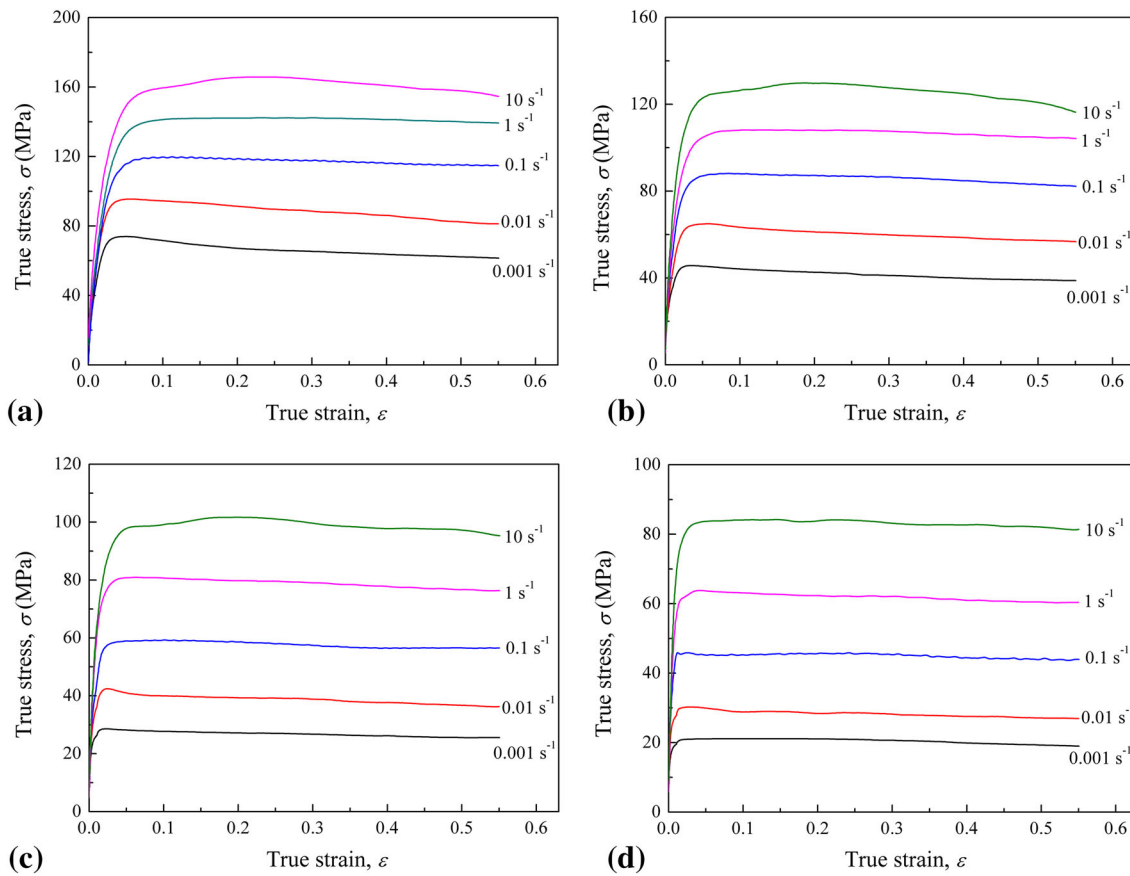
Fig. 4 True stress-strain curves of homogenized 2024 aluminum alloy with various strain rates and at the deformation temperatures of (a) 623 K, (b) 673 K, (c) 723 K, and (d) 773 K

stage. After that, the flow stress reaches to a peak value and then keeps constant or decreases slightly. As is known, this phenomenon is due to the fact that the deformation at elevated temperature is a competing process between work hardening and dynamic softening (Ref 26, 27). Moreover, it is obvious that both of the peak and steady flow stress is sensitive to deformation temperature and strain rate. The flow stress significantly decreases at higher deformation temperature, since the thermal activation processes becomes intense by raising the temperature. On the other hand, the flow stress is enhanced by increasing the strain rate, which can be explained by the rapid rise of dislocation generation and multiplication at higher strain rates (Ref 28). Importantly, it should be noticed that under the same deformation condition the flow stress at homogenized state is always higher compared with the as-cast one. As mentioned above, although some amount of GB phases was formed during the slow cooling, the GB phases with low melting temperature dissolves during homogenization, which leads to a higher degree of solid solution. Therefore, the effect of solid solution strengthening becomes notable in homogenized state, which causes strong resistance on dislocation motion and further increase of the magnitude of flow stress.

3.3 Constitutive Modeling

Several empirical models have been developed to derive the constitutive equation for metallic materials. Arrhenius model with high accuracy prediction of the flow stress is mostly used, since the coupled effects of strain rate and temperature are well considered in this model. The relationship between flow stress and deformation parameters can be expressed as,

$$\dot{\varepsilon} = A_1 \sigma^{n_1} \exp\left(-\frac{Q}{RT}\right) \tag{Eq 1}$$

$$\dot{\varepsilon} = A_2 \exp(\beta\sigma) \exp\left(-\frac{Q}{RT}\right) \tag{Eq 2}$$

$$\dot{\varepsilon} = A[\sinh(\alpha\sigma)]^n \exp\left(-\frac{Q}{RT}\right), \tag{Eq 3}$$

where $\dot{\varepsilon}$ is the strain rate, σ is the flow stress, Q is the activation energy of hot deformation, R is the universal gas constant, T is the absolute temperature, and A_1, A_2, n_1, β, and α are the material constants. It is generally accepted that the power law of Eq 1 could be used to describe the low stress ($\alpha\sigma < 0.8$), while the exponential law of Eq 2 could be used in high stress level ($\alpha\sigma > 1.2$). The hyperbolic sine-typed equation of Eq 3 is suitable for the entire range of stress, and the material constants of α can be calculated by β/n_1.

The influence of temperature and strain rate on the hot deformation behavior can be described by an exponent-typed Zener-Holloman parameter (Z) (Ref 29):

$$Z = \dot{\varepsilon} \exp\left(\frac{Q}{RT}\right). \tag{Eq 4}$$

By introducing Eq 4 into Eq 3, it yields another form of the Zener-Holloman parameter:

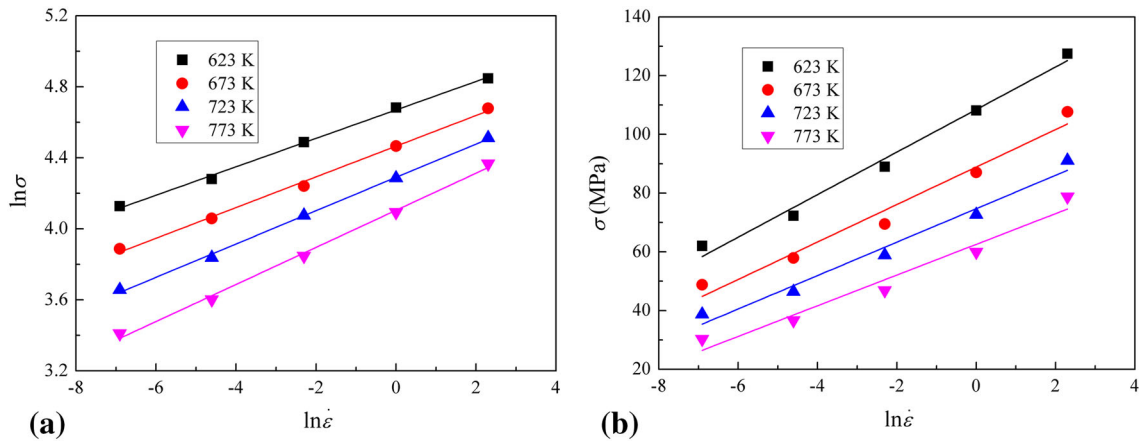**Fig. 5** Relationships of (a) ln ε̇-lnσ; (b) ln ε̇-σ

$$Z = A[\sinh(\alpha\sigma)]^n. \tag{Eq 5}$$

Besides, the flow stress σ can also be written as a function of Z by solving Eq 5 using the definition of hyperbolic sine function:

$$\sigma = \frac{1}{\alpha}\ln\left\{\left(\frac{Z}{A}\right)^{1/n} + \left[\left(\frac{Z}{A}\right)^{2/n} + 1\right]^{1/2}\right\}. \tag{Eq 6}$$

In this section, the constitutive equations based on Arrhenius model for as-cast and homogenized 2024 aluminum alloy are modeled. The peak flow stress is used to calculate the required material constants, and the detailed solving method is given below using the as-cast state as an example.

The following equations can be derived by taking the natural logarithm of both sides of Eq 1 and 2:

$$\ln\dot{\varepsilon} = \ln A_1 + n_1\ln\sigma - \frac{Q}{RT} \tag{Eq 7}$$

$$\ln\dot{\varepsilon} = \ln A_2 + \beta\sigma - \frac{Q}{RT}. \tag{Eq 8}$$

Then, n_1 and β can be obtained from Eq 7 and 8, once the flow stress and the corresponding strain rate are known. Figure 5 shows the relationship of ln ε̇-lnσ and ln ε̇-σ under different deformation temperatures. From the figure, it can be

seen that flow stresses are well fitted by a group of straight lines. The average reciprocal of the slopes of the lines in Fig. 5(a) and (b) can be used to calculate the value of n_1 and β, which is 11.0734 and 0.165 MPa^{-1}, respectively. Thus, the value of α, 0.015 MPa^{-1} can also be determined.

In order to get the activation energy Q, partial differential equation of Eq 3 is taken:

$$Q = R\left[\frac{\partial\ln\dot{\varepsilon}}{\partial\ln[\sinh(\alpha\sigma)]}\right]_T\left[\frac{\partial\ln[\sinh(\alpha\sigma)]}{\partial(1/T)}\right]_{\dot{\varepsilon}}. \tag{Eq 9}$$

Since the value of α has been derived, two relationships of ln ε̇-ln[sinh(ασ)] and 1/T-ln[sinh(ασ)] can be easily obtained, as plotted in Fig. 6. The value of $\partial\ln\dot{\varepsilon}/\partial[\ln\sinh(\alpha\sigma)]$ is derived by calculating the reciprocal of slopes of straight lines depicted in Fig. 6(a). Similarly, the value of $\partial[\ln\sinh(\alpha\sigma)]/\partial(1/T)$ can be derived by calculating the slopes of lines shown in Fig. 6(b). Based on Eq 9, the calculated activation energy Q of as-cast 2024 aluminum alloy is around 180.102 kJ mol^{-1}.

The values of material constants of n and A can be derived by taking the natural logarithm on both sides of Eq 5:

$$\ln Z = \ln A + n\ln[\sinh(\alpha\sigma)]. \tag{Eq 10}$$

The Z parameter under a given stain rate and deformation temperature could be evaluated by putting the value of Q into Eq 4. Figure 7 gives the linear relationship between lnZ and ln[sinh(ασ)]. According to Eq 10, the slope and intercept of the
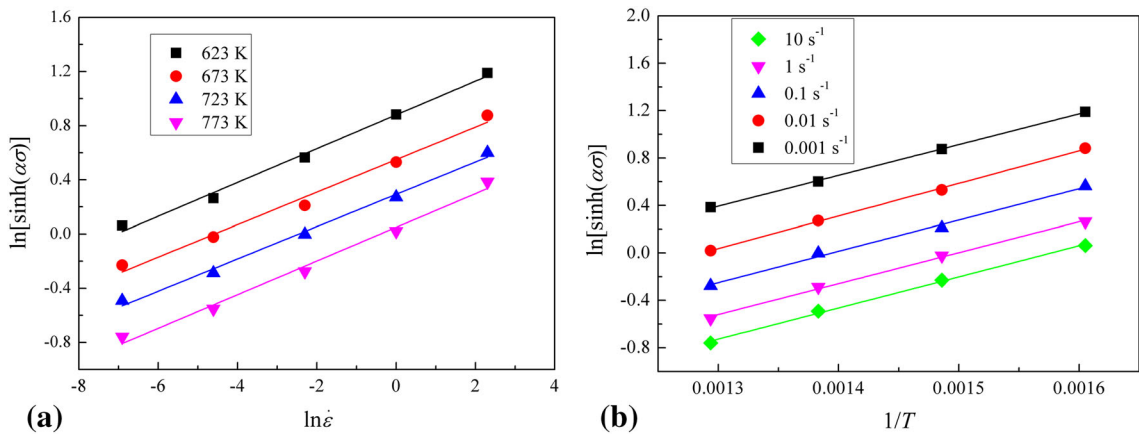

Fig. 6 Relationships of (a) ln ε̇-ln[sinh(ασ)] and (b)1/T -ln[sinh(ασ)]

fitting line in Fig. 7 were used to derive the values of n and $\ln A$, which are 8.152 and 27.612, respectively.

Following the similar way, material constants of homogenized 2024 aluminum alloy also can be derived. The material constants derived using peak stress for both initial sates are summarized in Table 1. As is known, Q is an important physical parameter indicating the deformation difficulty degree during the plastic deformation. In this paper, the sample in homogenized state shows higher Q value (218.384 kJ mol^{-1}) than that in as-cast state (180.102 kJ mol^{-1}). One possible explanation for this phenomenon is the solid solution strengthening works more effectively in homogenized state and the dislocation motion is strongly limited then. In addition, the Q values of both initial states are higher than that of the self-diffusion of pure aluminum (142 kJ mol^{-1}) (Ref 11). The main reason is that the stress used for derivation of activation energy is not normalized by Young's modulus, resulting in inconsistency of Q between these two kinds of alloys (Ref 30, 31). Moreover, the addition of alloying elements in 2024 aluminum alloy also plays an important role in increasing the activation energy due to the solution strengthening and solute drag effect.

Finally, according to Eq 6, the flow stress of as-cast and homogenized 2024 aluminum alloy could be described using Eq 11 and 12, respectively.

$$\sigma = \frac{1}{0.015}$$
$$\ln\left\{ \left(\frac{Z}{9.813 \times 10^{11}}\right)^{1/8.152} + \left[\left(\frac{Z}{9.813 \times 10^{11}}\right)^{2/8.152} + 1\right]^{1/2} \right\},$$
(Eq 11)

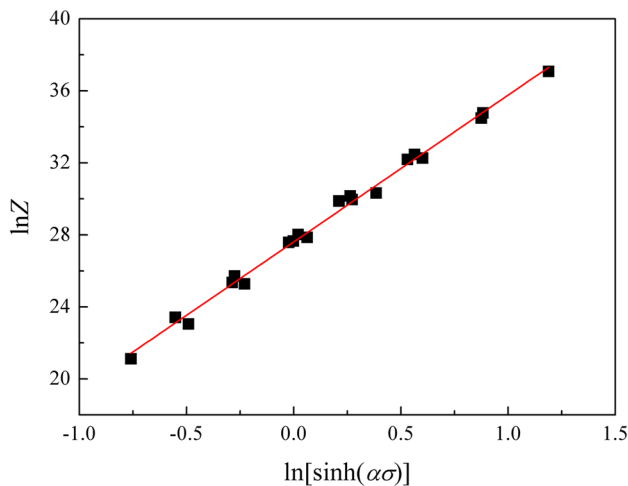where $Z = \dot{\varepsilon}\left(-\frac{1.801 \times 10^5}{RT}\right)$.

Fig. 7 Relationship between $\ln[\sinh(\alpha\sigma)]$ and $\ln Z$

Table 1 Material constants derived using peak stress for as-cast and homogenized 2024 aluminum alloy

Initial state	α, MPa^{-1}	Q, kJ mol^{-1}	n	$\ln A$
As-cast	0.015	180.102	8.152	27.612
Homogenized	0.014	218.384	6.060	34.297

$$\sigma = \frac{1}{0.014}$$
$$\ln\left\{ \left(\frac{Z}{7.852 \times 10^{14}}\right)^{1/6.060} + \left[\left(\frac{Z}{7.852 \times 10^{14}}\right)^{2/6.060} + 1\right]^{1/2} \right\},$$
(Eq 12)

where $Z = \dot{\varepsilon}\left(-\frac{2.184 \times 10^5}{RT}\right)$.

As can be seen, in the above model establishing process, the influence of the strain on the flow stress is not taken into account. However, the strain does affect the values of material constants. Hence, in order to enhance the prediction accuracy, the influence of the strain needs to be considered (Ref 10-13). The material constants of α, Q, n, and $\ln A$ in the strain range of 0.04-0.52 at an interval of 0.04 were calculated according to the method described above. Figure 8 shows the calculated results for both as-cast and homogenized 2024 aluminum alloy, which demonstrates that all material constants are greatly affected by the strain. The activation energy Q decreases gradually with the increase of the strain for both initial states, which indicates the deformation resistance becomes small. The reason has been reported that only a few slip systems are preferred orientation for slippage at the early deformation stage, while with the increasing strain, grain rotation results in activating more slip systems (Ref 30). The value of α tends to increase with the increase of the strain, while n and $\ln A$ show decreasing tendency. The balance between these material constants ensures an accuracy prediction on flow stress (Ref 32). Additionally, a fifth order polynomial fitting can be applied to well describe the relationship between the strain and the material constants, which can be expressed as,

$$\alpha = B_0 + B_1\varepsilon + B_2\varepsilon^2 + B_3\varepsilon^3 + B_4\varepsilon^4 + B_5\varepsilon^5$$
$$n = C_0 + C_1\varepsilon + C_2\varepsilon^2 + C_3\varepsilon^3 + C_4\varepsilon^4 + C_5\varepsilon^5$$
$$Q = D_0 + D_1\varepsilon + D_2\varepsilon^2 + D_3\varepsilon^3 + D_4\varepsilon^4 + D_5\varepsilon^5$$
$$\ln A = E_0 + E_1\varepsilon + E_2\varepsilon^2 + E_3\varepsilon^3 + E_4\varepsilon^4 + E_5\varepsilon^5.$$
(Eq 13)

Tables 2 and 3 list the fitting results of as-cast and homogenized 2024 aluminum alloy, respectively. Material constants under specified strain can be derived according to Eq 13, and the flow stress can be further calculated using Eq 6.

In the above analysis, constitutive equations of as-cast and homogenized 2024 aluminum alloy have been established based on Arrhenius model with and without strain compensation. In order to evaluate the accuracy of these modeled equations, the flow stresses at strain from 0.04 to 0.52 at an interval of 0.04 were calculated. Then, the predicted and experimental flow stresses are compared, as plotted in Fig. 9, where the solid line represents a perfect match. As is seen in Fig. 9(a) and (b), Arrhenius model only gives a rough estimation on the flow stress, since the influence of the strain on the flow stress was ignored. Moreover, it should be noticed that the flow stresses predicted by this model are usually overestimated. The reason is that the peak stress was selected for the calculation of material constants in this study. As shown in Fig. 9(c) and (d), a good agreement between predicted and experimental values is obtained when strain compensated Arrhenius model is applied for both initial states, which indicates an excellent predictability.

Moreover, the correlation coefficient (R) and AARE were calculated to provide quantitative evaluation on the accuracy of above established constitutive equations. The corresponding expressions are given as,
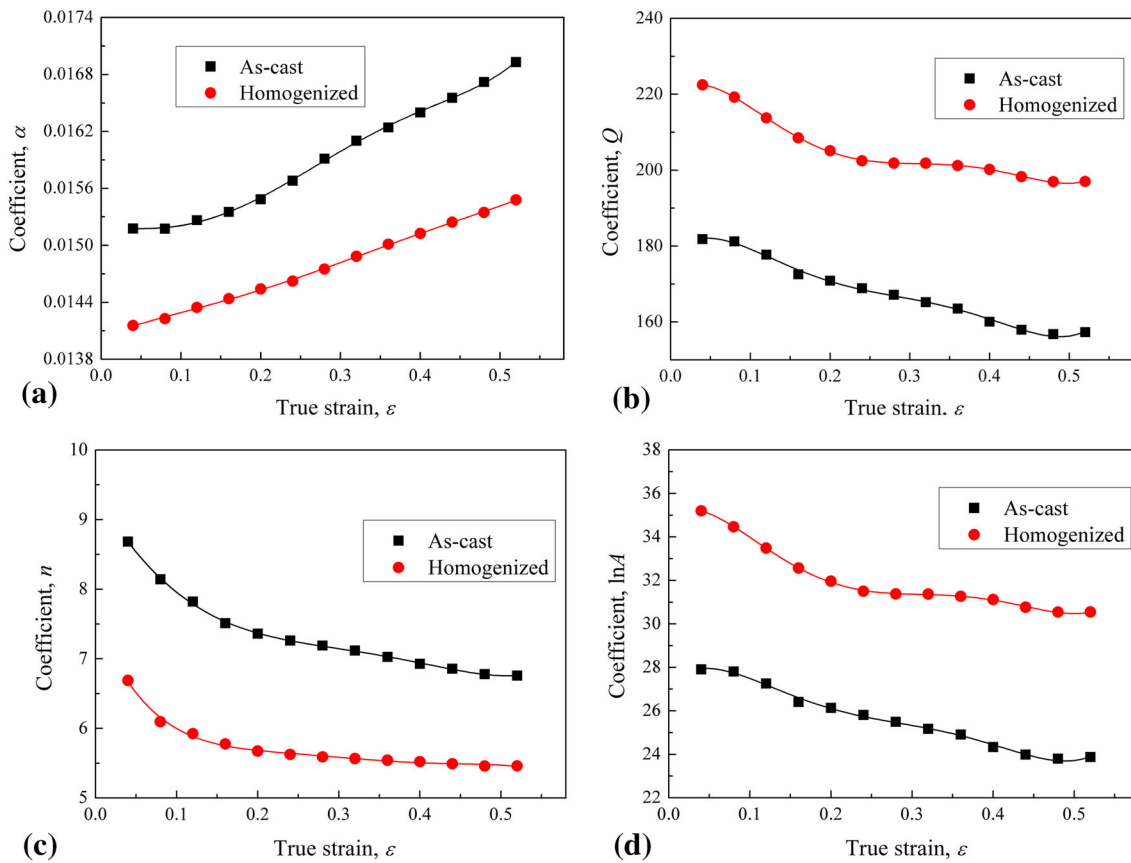
Fig. 8 Variations of material constants of (a) α, (b) Q, (c) n and (d) ln$A$ with strain for as-cast and homogenized 2024 aluminum alloy. (Solid lines represent the fifth order polynomial fitting lines)

Table 2 Polynomial fitting results for as-cast 2024 aluminum alloy

α	Q	n	ln$A$
$B_0 = 0.015$	$C_0 = 178.11$	$D_0 = 9.382$	$E_0 = 27.313$
$B_1 = 0$	$C_1 = 197.47$	$D_1 = -19.934$	$E_1 = 31.611$
$B_2 = 0.007$	$C_2 = -2994.6$	$D_2 = 62.838$	$E_2 = -477.31$
$B_3 = 0.153$	$C_3 = 13,866$	$D_3 = -49.849$	$E_3 = 2196.4$
$B_4 = -0.433$	$C_4 = -27,833$	$D_4 = -123.1$	$E_4 = -4393.1$
$B_5 = 0.367$	$C_5 = 20,301$	$D_5 = 177.88$	$E_5 = 3198.2$

Table 3 Polynomial fitting results for homogenized 2024 aluminum alloy

α	Q	n	ln$A$
$B_0 = 0.014$	$C_0 = 219.88$	$D_0 = 7.572$	$E_0 = 35.048$
$B_1 = 0.004$	$C_1 = 180.99$	$D_1 = -28.898$	$E_1 = 20.949$
$B_2 = -0.016$	$C_2 = -3522.9$	$D_2 = 180.07$	$E_2 = -530.64$
$B_3 = 0.077$	$C_3 = 16,887$	$D_3 = -567.54$	$E_3 = 2632.6$
$B_4 = -0.146$	$C_4 = -32,964$	$D_4 = 871.68$	$E_4 = -5200$
$B_5 = 0.098$	$C_5 = 22,923$	$D_5 = -518.62$	$E_5 = 3633.2$

$$R = \frac{\sum_{i=1}^{N}(E_i - \bar{E})(P_i - \bar{P})}{\sqrt{\sum_{i=1}^{N}(E_i - \bar{E})^2 \sum_{i=1}^{N}(P_i - \bar{P})^2}} \qquad \text{(Eq 14)}$$

$$\text{AARE (\%)} = \frac{1}{N}\sum_{i=1}^{N}\left|\frac{E_i - P_i}{E_i}\right| \times 100, \qquad \text{(Eq 15)}$$

where E_i and P_i are the experimental and predicted flow stresses, respectively, $\bar{E}$ and $\bar{P}$ are the mean values of E_i and P_i, and N is the number of data selected for calculation. R is used to reflect the strength of the linear relationship between experimental and predicted data, while AARE is considered as an unbiased statistical parameter to evaluate the predictability of equations. From the results given in Fig. 9, the values of R and AARE have been calculated and the results

are listed in Table 4. From Table 4, it is demonstrated that the strain compensated Arrhenius model for as-cast state sample exhibits the highest accuracy, where the values of R and AARE are 0.9976 and 2.6759%, respectively. More generally, strain compensated Arrhenius model always has higher R and smaller AARE values, which illustrates that the prediction accuracy has been greatly enhanced by introducing the strain compensation.

3.4 Processing Maps

According to the principle of DMM (Ref 14), the hot working could be considered as a dissipater of power. The total instantaneous power dissipation (P) consists of two complementary parts: G content and J co-content, and it can be expressed as a function of strain, strain rate and flow stress:
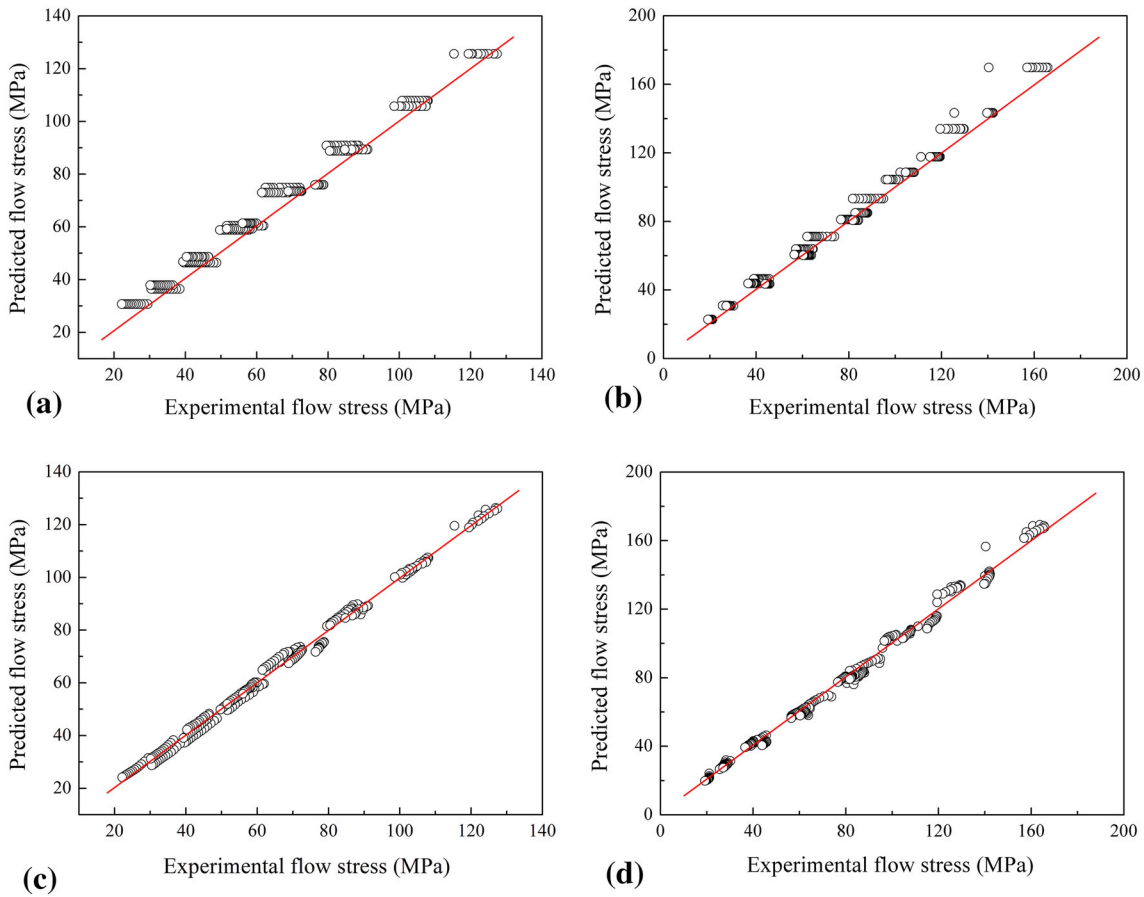
Fig. 9 Comparison between the experimental and predicted flow stresses: Arrhenius model for (a) as-cast state, (b) homogenized state; Strain compensated Arrhenius model for (c) as-cast state, (d) homogenized state

Table 4 Calculated values of R and ARRE for different constitutive models

Initial state	Arrhenius model		Strain compensated Arrhenius model	
	R	AARE, %	R	AARE, %
As-cast	0.9922	8.0521	0.9976	2.6759
Homogenized	0.9950	6.2289	0.9967	3.3946

$$P = \sigma\dot{\varepsilon} = G + J = \int_0^{\dot{\varepsilon}} \sigma d\dot{\varepsilon} + \int_0^{\sigma} \dot{\varepsilon} d\sigma, \qquad (\text{Eq } 16)$$

where G and J are corresponding to the power dissipation for temperature rise and microstructure transition during hot deformation, respectively. Moreover, the strain rate sensitivity (m) is used to partition the power into G content and J co-content (Ref 33), which can be expressed as,

$$m = \frac{dJ}{dG} = \frac{\partial(\ln\sigma)}{\partial(\ln\dot{\varepsilon})}. \qquad (\text{Eq } 17)$$

Under any specified strain rate and deformation, J co-content could be derived according to the following equation:

$$J = \int_0^{\sigma} \dot{\varepsilon} d\sigma = \frac{m\sigma\dot{\varepsilon}}{m+1}. \qquad (\text{Eq } 18)$$

For an ideal linear dissipater with $m = 1$, the J co-content has the maximum value ($J_{max} = \sigma\dot{\varepsilon}/2$). Thus, the power dissipation capacity of the material can be expressed by introducing a dimensionless parameter called the efficiency of power dissipation (η) (Ref 34), which is given by:

$$\eta = \frac{J}{J_{max}} = \frac{2m}{2m+1}. \qquad (\text{Eq } 19)$$

The parameter η represents the proportion of the power dissipated by microstructure changes to the total power. Higher η value means larger power which is dissipated by microstructure changes. Then, the power dissipation map can be obtained by plotting iso-efficiency contour lines of η on the temperature-strain rate field, from which different deformation mechanisms might be identified (Ref 26).

Generally, the material should have good workability in the domains at high η values. However, high η value does not always represent the optimum process condition, since the flow instabilities and cracking might occur. Therefore, based on the extreme principles of irreversible thermodynamics applied for large plastic flow body (Ref 33), the instability parameter ($\xi(\dot{\varepsilon})$) should be introduced to recognize the instable domain, which is expressed as:
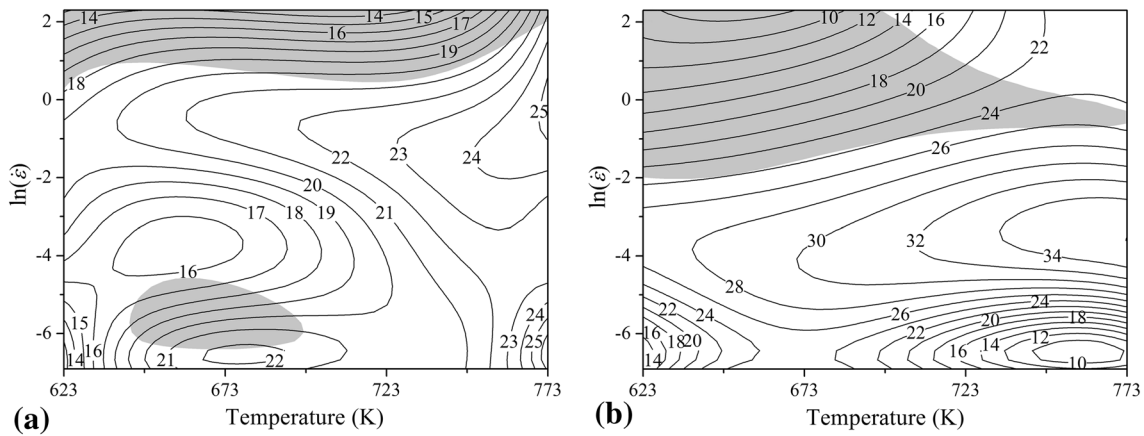
Fig. 10 Processing maps of 2024 aluminum of in (a) as-cast state and (b) homogenized state
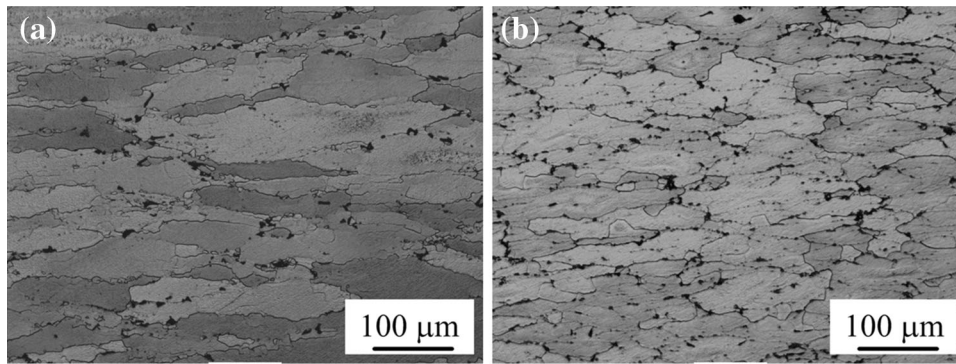

Fig. 11 Optical microstructures of 2024 aluminum alloy after deformation at 773 K and 0.01 s^{-1}: (a) as-cast state, (b) homogenized state

$$\xi(\dot{\varepsilon}) = \frac{\partial \ln(m/m + 1)}{\partial \ln \dot{\varepsilon}} + m < 0. \qquad \text{(Eq 20)}$$

The instability map could also be established by plotting the instability parameter $\xi(\dot{\varepsilon})$ on temperature-strain rate field, and the domains with negative values of $\xi(\dot{\varepsilon})$ indicate the flow instability.

According to the above theory, in the present study, the processing maps of as-cast and homogenized 2024 aluminum alloy at the strain of 0.55 were constructed by superposing the efficiency power dissipation map and the instability map, as shown in Fig. 10. The counter lines represent the constant efficiency of power dissipation in percentage, while the shadow area represents the instability domains ($\xi(\dot{\varepsilon}) < 0$). From Fig. 10, one general tendency can be observed that the efficiency of power dissipation increases with increasing deformation temperatures and decreasing strain rate. The climbing of edge dislocation and the crossing sliding of screw dislocation are accelerated at higher temperature, and it takes time to accumulate the dislocation density. Therefore, higher temperature and lower strain rate are beneficial for the triggering of microstructure transition, such as dynamic recovery and dynamic recrystallization, which leads to a higher efficiency (Ref 35). This can be verified by the microstructure of as-cast state (773 K, 0.01 s^{-1}) and homogenized state (773 K, 0.01 s^{-1}) shown in Fig. 11. As is seen, some newly formed

equiaxed grains can be found, which proves the occurrence of the dynamic recrystallization. Moreover, by comparing Fig. 11(a) and (b), it can also be found that the degree of dynamic recrystallization is higher in homogenized state than that in as-cast state. As the dynamic recrystallization can provide good intrinsic workability both by softening and reconstituting the microstructure, it is a beneficial process for hot working (Ref 36). This should be one possible reason for that the overall efficiency of power dissipation is higher in homogenized state than that in as-cast state.

As discussed above, it is also necessary to investigate the flow instabilities domains in order to determine the optimum hot working condition. For both initial states, the main instability domain is found at high strain rates, which locates at the upper part of processing maps, as shown in Fig. 10. Generally, the mechanisms of flow instabilities are probably associated with the adiabatic shear bands, flow localizations, dynamic strain aging, kinking, mechanical twinning, and flow rotations (Ref 37). Therefore, the deformation temperatures and strain rates in the instability domain should be avoided during the practical hot forming process. Accordingly, the hot forming process is suggested to be carried out at the temperature range of 710-773 K and at strain rate range of 0.001-1 s^{-1} for as-cast state with a peak power dissipation of 26.8%, and for homogenized state, the temperature range of 680-773 K and the strain rate range of 0.003-0.22 s^{-1} with a peak power dissipation of 36.1% is suggested.

4. Conclusions

A comparable study on constitutive equations and processing maps of as-cast and homogenized 2024 aluminum alloy was carried out by means of hot compression tests. From the results, the following conclusions could be drawn.

1. The homogenized 2024 aluminum alloy shows higher flow stress compared with the as-cast state, due to its higher degree of solid solution strengthening. Moreover, the flow behavior is sensitive to both the deformation temperature and strain rate. The flow stress increases with the increase of strain rate and the decrease of deformation temperature.
2. Constitutive equations based on Arrhenius model with and without strain compensation were established for 2024 aluminum alloy, respectively. By comparison of the values of R and AARE calculated from two models, it can be obviously seen that Arrhenius model without strain compensation only provides a rough estimation of the flow stress. Once taking the influence of strain on material constants into account, the prediction accuracy could be greatly enhanced.
3. Processing maps of the as-cast and homogenized 2024 aluminum alloy were established based on DMM. Accordingly, the hot forming process is suggested to be conducted at the temperature range of 710-773 K and strain rate range of 0.001-1 s^{-1} for as-cast state, while for homogenized state the suggested temperature range is 680-773 K and strain rate range is 0.003-0.22 s^{-1}.

References

1. Y.C. Lin, Y.C. Xia, X.S. Ma, Y.Q. Jiang, and M.S. Chen, High-Temperature Creep Behavior of Al-Cu-Mg Alloy, *Mater. Sci. Eng., A*, 2012, **550**, p 125–130
2. H.R. Rezaei Ashtiani, M.H. Parsa, and H. Bisadi, Constitutive Equations for Elevated Temperature Flow Behavior of Commercial Purity Aluminum, *Mater. Sci. Eng. A*, 2012, **545**, p 61–67
3. L. Chen, G. Zhao, J. Yu, W. Zhang, and T. Wu, Analysis and Porthole Die Design for a Multi-hole Extrusion Process of a Hollow, Thin-Walled Aluminum Profile, *Int. J. Adv. Manuf. Tech.*, 2014, **74**, p 383–392
4. C. Zhang, G. Zhao, H. Chen, Y. Guan, H. Cai, and B. Gao, Investigation on Effects of Die Orifice Layout on Three-Hole Porthole Extrusion of Aluminum Alloy 6063 Tubes, *J. Mater. Eng. Perform.*, 2013, **22**, p 1223–1232
5. H.S. Liu, J. Bao, Z.W. Xing, D.J. Zhang, B.Y. Song, and C.X. Lei, Modeling and FE Simulation of Quenchable High Strength Steels Sheet Metal Hot Forming Process, *J. Mater. Eng. Perform.*, 2011, **20**, p 894–902
6. Y.C. Lin, Y.Q. Jiang, H.M. Zhou, and G. Liu, A New Creep Constitutive Model for 7075 Aluminum Alloy Under Elevated Temperatures, *J. Mater. Eng. Perform.*, 2014, **23**, p 4350–4357
7. Y. Deng, Z. Yin, and J. Huang, Hot Deformation Behavior and Microstructural Evolution of Homogenized 7050 Aluminum Alloy During Compression at Elevated Temperature, *Mater. Sci. Eng., A*, 2011, **528**, p 1780–1786
8. M.A. Jabbari Taleghani, E.M. Ruiz Navas, M. Salehi, and J.M. Torralba, Hot Deformation Behaviour and Flow Stress Prediction of 7075 Aluminium Alloy Powder Compacts During Compression at Elevated Temperatures, *Mater. Sci. Eng. A*, 2012, **534**, p 624–631
9. L. Hua, F. Meng, Y. Song, J. Liu, X. Qin, and Lianbing Suo, A Constitutive Model of 6111-T4 Aluminum Alloy Sheet Based on the Warm Tensile Test, *J. Mater. Eng. Perform.*, 2014, **23**, p 1107–1113
10. Y.C. Lin, Y.C. Xia, X.M. Chen, and M.S. Chen, Constitutive Descriptions for Hot Compressed 2124-T851 Aluminum Alloy over a Wide Range of Temperature and Strain Rate, *Comp. Mater. Sci.*, 2010, **50**, p 227–233
11. J.C. Shao, B.L. Xiao, Q.Z. Wang, Z.Y. Ma, Y. Liu, and K. Yang, Constitutive Flow Behavior and Hot Workability of Powder Metallurgy Processed 20vol.%SiCP/2024Al Composite, *Mater. Sci. Eng., A*, 2010, **527**, p 7865–7872
12. M.R. Rokni, A. Zarei-Hanzaki, C.A. Widener, and P. Changizian, The Strain-Compensated Constitutive Equation for High Temperature Flow Behavior of an Al-Zn-Mg-Cu Alloy, *J. Mater. Eng. Perform.*, 2014, **23**, p 4002–4009
13. L. Chen, G. Zhao, J. Yu, and W. Zhang, Constitutive Analysis of Homogenized 7005 Aluminum Alloy at Evaluated Temperature for Extrusion Process, *Mater. Des.*, 2015, **66**, p 129–136
14. Y.V.R.K. Prasad, H.L. Gegel, S.M. Doraivelu, J.C. Malas, J.T. Morgan, K.A. Lark, and D.R. Barker, Modeling of Dynamic Material Behavior in Hot Deformation Forging of Ti-6242, *Metall. Mater. Trans. A*, 1984, **15A**, p 1883–1892
15. Y. Kong, P. Chang, Q. Li, L. Xie, and S. Zhu, Hot Deformation Characteristics and Processing Map of Nickel-Based C276 Superalloy, *J. Alloys Comp.*, 2015, **622**, p 738–744
16. A.K. Maheshwari, K.K. Pathak, N. Ramakrishnan, and S.P. Narayan, Modified Johnson-Cook Material Flow Model for Hot Deformation Processing, *J. Mater. Sci.*, 2009, **45**, p 859–864
17. M. Rajamuthamilselvan and S. Ramanathan, Hot Deformation Behaviour of 7075 Alloy, *J. Alloys Comp.*, 2011, **509**, p 948–952
18. S. Banerjee, P.S. Robi, and A. Srinivasan, Deformation Processing Maps for Control of Microstructure in Al-Cu-Mg Alloys Microalloyed with Sn, *Metall. Mater. Trans. A*, 2012, **43**, p 3834–3849
19. V. Senthilkumar, A. Balaji, and R. Narayanasamy, Analysis of Hot Deformation Behavior of Al 5083-TiC Nanocomposite Using Constitutive and Dynamic Material Models, *Mater. Des.*, 2012, **37**, p 102–110
20. S.B. Bhimavarapu, A.K. Maheshwari, D. Bhargava, and S.P. Narayan, Compressive Deformation Behavior of Al 2024 Alloy Using 2D and 4D Processing Maps, *J. Mater. Sci.*, 2011, **46**, p 3191–3199
21. M. Wang, P. Jin, J. Wang, and L. Han, Hot Deformation Behavior of As-Quenched 7005 Aluminum Alloy, *T. Nonferr. Metal. Soc.*, 2014, **24**, p 2796–2804
22. B.L. Xiao, J.Z. Fan, X.F. Tian, W.Y. Zhang, and L.K. Shi, Hot Deformation and Processing Map of 15%SiCp/2009 Al Composite, *J. Mater. Sci.*, 2005, **40**, p 5757–5762
23. J.C. Malas, S. Venugopal, and T. Seshacharyulu, Effect of Microstructural Complexity on the Hot Deformation Behavior of Aluminum Alloy 2024, *Mater. Sci. Eng., A*, 2008, **368**, p 41–47
24. G.R. Ebrahimi, A. Zarei-Hanzaki, M. Haghshenas, and H. Arabshahi, The Effect of Heat Treatment on Hot Deformation Behaviour of Al 2024, *J. Mater. Process. Technol.*, 2008, **206**, p 25–29
25. A.R. Eivani, H. Ahmed, J. Zhou, and J. Duszczyk, Evolution of Grain Boundary Phases During the Homogenization of AA7020 Aluminum Alloy, *Metall. Mater. Trans. A*, 2009, **40**, p 717–728
26. B. Li, Q. Pan, and Z. Yin, Characterization of Hot Deformation Behavior of As-Homogenized Al-Cu-Li-Sc-Zr Alloy Using Processing Maps, *Mater. Sci. Eng., A*, 2014, **614**, p 199–206
27. Y. Zhang, S. Jiang, Y. Zhao, and D. Shan, Isothermal Precision Forging of Complex-Shape Rotating Disk of Aluminum Alloy Based on Processing Map and Digitized Technology, *Mater. Sci. Eng., A*, 2013, **580**, p 294–304
28. A. Abbasi-Bani, A. Zarei-Hanzaki, M.H. Pishbin, and N. Haghdadi, A Comparative Study on the Capability of Johnson-Cook and Arrhenius-Type Constitutive Equations to Describe the Flow Behavior of Mg-6Al-1Zn Alloy, *Mech. Mater.*, 2014, **71**, p 52–61
29. C. Zener and J.H. Hollomon, Effect of Strain Rate Upon Plastic Flow of Steel, *J. Appl. Phys.*, 1944, **15**, p 22–32

30. Z. Yang, F. Zhang, C. Zheng, M. Zhang, B. Lv, and L. Qu, Study on Hot Deformation Behaviour and Processing Maps of Low Carbon Bainitic Steel, *Mater. Des.*, 2015, **66**, p 258–266

31. L. Wang, F. Liu, J.J. Cheng, Q. Zuo, and C.F. Chen, Hot Deformation Characteristics and Processing Map Analysis for Nickel-Based Corrosion Resistant Alloy, *J. Alloys Comp.*, 2015, **623**, p 69–78

32. C. Liao, H. Wu, C. Wu, F. Zhu, and S. Lee, Hot Deformation Behavior and Flow Stress Modeling of Annealed AZ61 Mg Alloys, *Prog. Nat. Sci.*, 2014, **24**, p 253–265

33. Y.V.R.K. Prasad and T. Seshacharyulu, Processing Maps for Hot Working of Titanium Alloys, *Mater. Sci. Eng., A*, 1998, **243**, p 82–88

34. Y.V.R.K. Prasad and T. Seshacharyulu, Modelling of Hot Deformation for Microstructural Control, *Int. Mater. Rev.*, 1988, **43**, p 243–258

35. Y. Yang, Z. Zhang, and X. Zhang, Processing Map of Al_2O_3 Particulate Reinforced Al Alloy Matrix Composites, *Mater. Sci. Eng., A*, 2012, **558**, p 112–118

36. Y. Yang, Z. Zhang, X. Li, Q. Wang, and Y. Zhang, The Effects of Grain Size on the Hot Deformation and Processing Map for 7075 Aluminum Alloy, *Mater. Des.*, 2013, **51**, p 592–597

37. Y.C. Lin, L.T. Li, Y.C. Xia, and Y.Q. Jiang, Hot Deformation and Processing Map of a Typical Al-Zn-Mg-Cu Alloy, *J. Alloys Comp.*, 2013, **550**, p 438–445